Spectrum of Engineering Sciences
ISSN (e) 3007-3138 **(p)** 3007-312X Volume 3, Issue 11, 2025

MACHINE LEARNING-DRIVEN PREDICTION OF BUCKLING RESPONSE IN TUBULAR STRUCTURES VIA FINITE ELEMENT-GENERATED DATA

Dr. M. Adil Khan*[1], Masaud Ahmad Khan[2], Ghulam Yameen Mallah[3], Engr. Baitullah Khan Kibzai[4], Muhammad Munawar[5], Engr. Muhammad Rauf[6], Uzair Ali[7]

[1]Resident Engineer (RE), National Engineering Services Pakistan (NESPAK), Lahore, Pakistan.
[2]CECOS University of IT and Emerging Sciences, Peshawar, Pakistan.
[3]Basic science and related studies, Quaid-e-Awam University of Engineering Science and Technology, Nawabshah, Pakistan.
[4]Senior Engineer, PCSIR KLC, Karachi, Pakistan.
[5]Local Government, Elections and Rural Development Department, Khyber Pakhtunkhwa, Pakistan.
[6]The University of Lahore, Lahore, Pakistan.
[7]Local Government and Rural Development Department, Khyber Pakhtunkhwa, Pakistan.

[1]adee.uol@gmail.com, [2]engrmasaudkh@gmail.comz, [3]gh.yameen@quest.edu.pk, [4]bkk_rulz@yahoo.com, [5]sdomunawartma@gmail.com, [6]raufcivilengr097@gmail.com, [7]engruzair91@gmail.com

DOI: https://doi.org/

Keywords
Investor-State Disputes, Treaty Modernization, Foreign Investment Regulation, Bilateral Investment Treaties, Sovereign Control, Arbitration Consent.

Article History
Received on 20 September 2025
Accepted on 02 October 2025
Published on 27 October 2025

Corresponding Author: *
Dr. M. Adil Khan*

Abstract

This paper presents a machine-learning method for predicting buckling in tubular structures. A comprehensive set of force-time histories is generated within a design space characterized by highly nonlinear buckling behavior, using a calibrated finite element model. The neural network is fully connected, with key hyperparameters optimized before testing on an unknown dataset. This dataset includes measurements such as peak load, average load, and energy absorption error. The results show systematic rather than random simple error patterns that correspond with the physical process of structural collapse. To confirm this, finite-element simulations are performed with various geometric imperfections. These errors show similar properties, and the neural network's error characteristics are analyzed in detail through force-time curve comparison. The deviations from the neural network are found to have physical significance. Overall, the results suggest that this approach can reliably replicate crushing behavior, with sufficient accuracy to account for minor differences caused by small geometric defects.

INTRODUCTION

Numerous fields, including aeronautical, automotive, and marine engineering, rely on thin-walled tubular structures to absorb energy under dynamic impact loading (Xu et al., 2023). They are mostly metal and can be deformed plastically to absorb kinetic energy (Wang et al., 2022). In 1960, Alexander created analytical estimations of the mean force and the fold length, which led to the investigation of the fundamental crushing process of tubes (Anand et al., 2024). Many further investigations into the dynamics of the deformation process have yielded analytical equations for the development of folds in relation to the deformation mode and their geometric properties (Zhang et al., 2025). Their dynamic response was discovered to be significantly affected by their height and cross-sectional properties. The dynamic collapse response and buckling mode transition of circular tubes were the subject of comprehensive research by Zhang et al. (2021). Impact speed and activated buckling modes were found to have a significant impact on the reaction and energy absorption during crushing for a particular design. A global buckling response and a progressive crushing response are the two main categories into which the mechanical response falls. The second option results in much reduced energy absorption, and Sun et al. (2021) also confirmed that the critical buckling length is affected by the impact velocity. In progressive crushing, simple geometric changes, such as adjusting the tube length, can lead to the emergence of multiple folding modes (in addition to axisymmetric crushing). An optimal design for one loading condition might lead to a suboptimal design for another loading scenario, for instance, for a different loading speed, due to the existence of such phenomena, which Sun et al. (2021) noted greatly complicates the design of energy-absorbing structures. Experiments can only cover a limited number of design situations because of practical constraints. To examine expansive parameter spaces, numerical simulations are usually employed instead. The dynamic folding and buckling of tubular structures have been extensively studied using finite element modeling. Nevertheless, the exploration of expansive design spaces through finite element simulations may be hindered by high numerical costs, which are caused by the requirement of fine meshes and small-time steps to ensure solution stability and accuracy (Schneider et al., 2022). In optimization studies of complicated energy-absorbing structures, these computational cost issues are

especially problematic (Sun et al., 2025). For instance, specialized methods are often used to reduce processing costs; however, these methods decrease the accuracy of the results produced. Building surrogate modeling methodologies is a viable alternative to nonlinear dynamic analysis, which requires a large amount of processing resources and a large number of simulations to account for loading input errors. Because recent studies on crashworthiness have focused on ever-expanding parametric spaces, for example, Gara et al. (2023) examined the impact of non-metallic materials on deformation mechanisms. Moreover, Najm et al. (2021) examined the effects of eccentric loading and also examined the design of metamaterials. The use of artificial neural networks (ANN) to simulate various nonlinear mechanical processes has grown in popularity. The system properties that need to be captured have dictated the ANN architecture used. Predicting the structural response of thin marine or civil structures and identifying modeling factors, such as damping, are two examples of applications of feed-forward networks (FFNs) (Alrowais et al., 2023). Recurrent neural networks and other more sophisticated designs are seeing use in civil engineering and impact loading identification (Sakaridis et al., 2022). To forecast the crash reaction in different parametrized structural designs, Zeng et al. (2024) utilized fully connected neural network models within the framework of crashworthiness. A comparable approach was employed by Li et al. (2025) to characterize the behavior of the anti-climbing device. When optimizing a combined energy absorber structure, Najibi et al. (n.d) used neural networks as surrogate models to reflect crashworthiness criteria, including peak load and specific energy absorption. To combine the computational economy of analytical approaches with the accuracy of finite element simulations, we investigate the possibility of employing machine learning to predict the dynamic crushing and buckling mode transition of tubular structures in this work. Using finite element simulations based on previous studies (Fernandez-Navamuel et al., 2022), an extensive dataset of force-displacement curves is created by varying both the structural attributes of the mechanical system (tube height) and the applied loading parameters (impact velocity). This dataset covers a variety of global buckling and progressive crushing modes. The paper lays out the steps for training and validating models based on machine learning and proposes an architecture for feed-forward neural networks. We find the training hyperparameters that enable the neural network model to excel at predicting the dynamic, highly nonlinear crushing reaction. Measures derived from engineering practice in crashworthiness

applications are used to assess the trained model's performance on a different test set. Next, the response variance due to small changes in the number of geometric defects is compared to the consequent mistakes.

2. Generation of training data

This research aims to predict the force-displacement response of tubular structures during impact events. To achieve this, we train neural networks on data produced by finite element simulations.

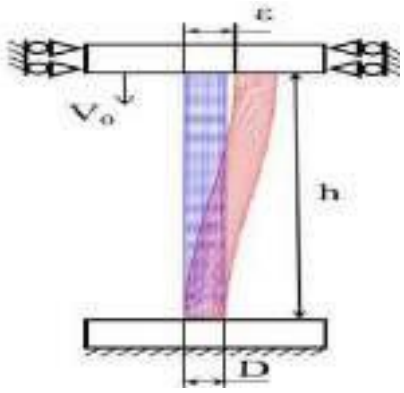

Figure 1: Finite element model, Schematic representation

2.1. Finite element models

The numerical models for tubular structures in this study are derived from the foundational work of Karagiozova et al. (2000), who systematically investigated the transition between progressive buckling and global dynamic collapse modes. The simulation matrix encompasses tubes with a fixed cross-section, an external diameter (D_0) of 50.8 mm, and a wall thickness (t) of 2 mm, but with heights (h) varying from 732 mm to 732 mm, subjected to impact velocities (V_0) ranging from 3 to 13 m/s. The axial crushing process was simulated using the commercial finite element package ABAQUS/Explicit (Ataabadi et al., 2022). The model configuration featured a deformable tube positioned between two rigid plates; the bottom plate was fixed, while the top plate, assigned a mass to yield a constant initial kinetic energy of 5 kJ, was given an initial velocity (V_0). To ensure computational accuracy in capturing the complex folding patterns, the tube was discretized with S4R shell elements. The element size was carefully selected based on an analytical estimation of the axisymmetric folding wavelength, which was calculated to be approximately δ = 19.8 mm (Author, Year). A longitudinal element size of 3 mm ($\approx\delta/6$) and a slightly larger peripheral size of 3.9 mm were consequently implemented. Furthermore, small geometric imperfections, introduced via the first two elastic buckling modes with a magnitude of $\varepsilon = 0.0005h$, were incorporated to promote realistic buckling behavior, a value consistent with tolerances for extruded aluminum tubes (Author, Year). The aluminum material was modeled using a rate-independent J2-plasticity model with isotropic hardening, defined by a Young's modulus of 70 GPa, a Poisson's ratio of 0.35, an

initial yield stress of 175 MPa, and a hardening modulus of 500 MPa. This robust finite element model was then employed to generate a comprehensive dataset for machine learning. A total of 5,000 distinct simulations were executed by randomly sampling the input parameter space of h and V_0. The resulting force-time histories from each simulation were standardized to a uniform length of 5,000 data points via zero-padding, a preprocessing step that obscures the crushing termination point and compels the neural network to learn the underlying physics. The final dataset, comprising 25 million data points of the form {h, V_0, t, F}, was partitioned into training (81%), validation (9%), and testing (10%) subsets. The primary objective of the neural network modeling is to establish a surrogate function capable of predicting the force-displacement response. Subsequently, the acceleration history can be deduced from the predicted force, and the top plate displacement can be obtained through numerical integration, thereby providing a complete dynamic response prediction.

$$\delta \cong 2\sqrt{Dt} \qquad (1)$$

2.2 Datasets

The neural network is trained using the datasets developed with the help of the finite element model. There are two variables in the input design space: tube height and impact velocity, which range between 244 and 732 millimeters and 3 and 13 meters per second, respectively. Combinations of (h) and (V0) within this range are randomly sampled to give a total of 5000 unique simulations. Every simulation generates a force-time response that reflects the crushing behavior of the tube during impact. In each instance, the simulation will continue until the loading plate comes to a complete halt (its velocity is zero) or 5000-time steps have been completed, which is approximately 0.12 seconds in real physical time. The force-time histories (F(t)) are standardized to a length of 5000 points to prepare their neural network input. Some curves that are shorter than this are padded with a zero on the end. This padding ensures that the network does not infer the cessation of crushing based directly on the sequence length, and thus learning is enforced through the behavior of the force response rather than the length of the curve. The last dataset will be around 25 million data points, which are in the form of ({h, V0, t, F). This total number of 5,000 force-time curves is separated into three mutually exclusive subsets: 4,050 force-time curves for training, 450 for validation, and 500 for testing, which represent approximately 81

percent, 9 percent, and 10 percent of the entire dataset, respectively (as shown in Figs. 2a-2c). Every subset has its own complete history of forces, providing model evaluation with unbiasedness.

$$\Delta t_s = \frac{h_{\min}}{2\sqrt{\frac{E}{\rho}}}$$

3.1. Neural network model architecture

Though it is known that recurrent neural networks like LSTMs work effectively in tasks where time-dependent dynamics are involved, their benefits are not as obvious in this scenario since the impact issues at hand do not offer a sequence input structure in any meaningful way. Thus, this paper is limited to the standard feed-forward fully connected neural network structures (see Fig. 3).

$$f_{NN} : \{t_n, h, V_0\} \rightarrow \{F_n\}$$

All variations of the network architecture comprise an input layer, containing the aforementioned input values, a variable number of hidden layers, ranging from 3 to 12, and a linear output layer that delivers the force value. For the activation function for the hidden layers, we consider the hyperbolic tangent (tanh) and the Rectified Linear Unit (ReLU) functions. The size of the hidden layers considered ranges from 40 to 180 neurons per layer, with an increment of 20 neurons. In all investigated architectures, the number of neurons per layer is the same for all hidden layers.

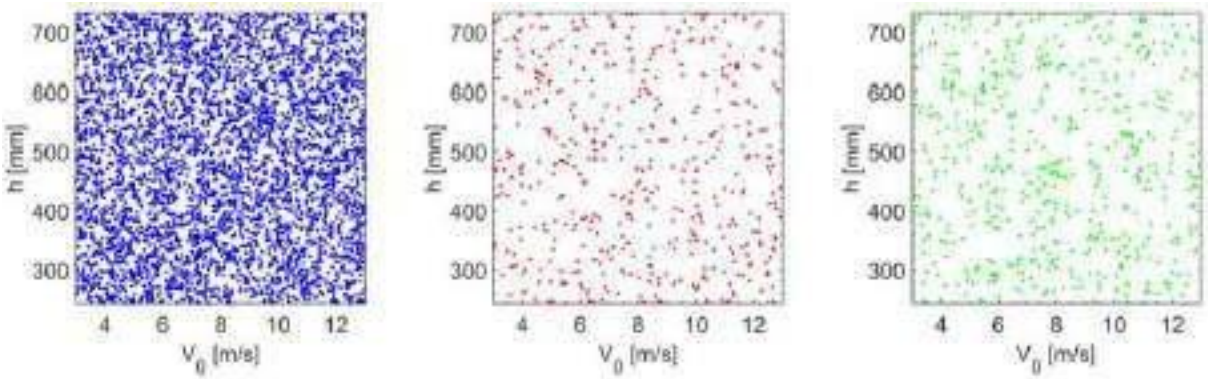

Fig. 2. Training dataset points (a, left), Validation dataset points (b, middle) and Test dataset points (c, right).

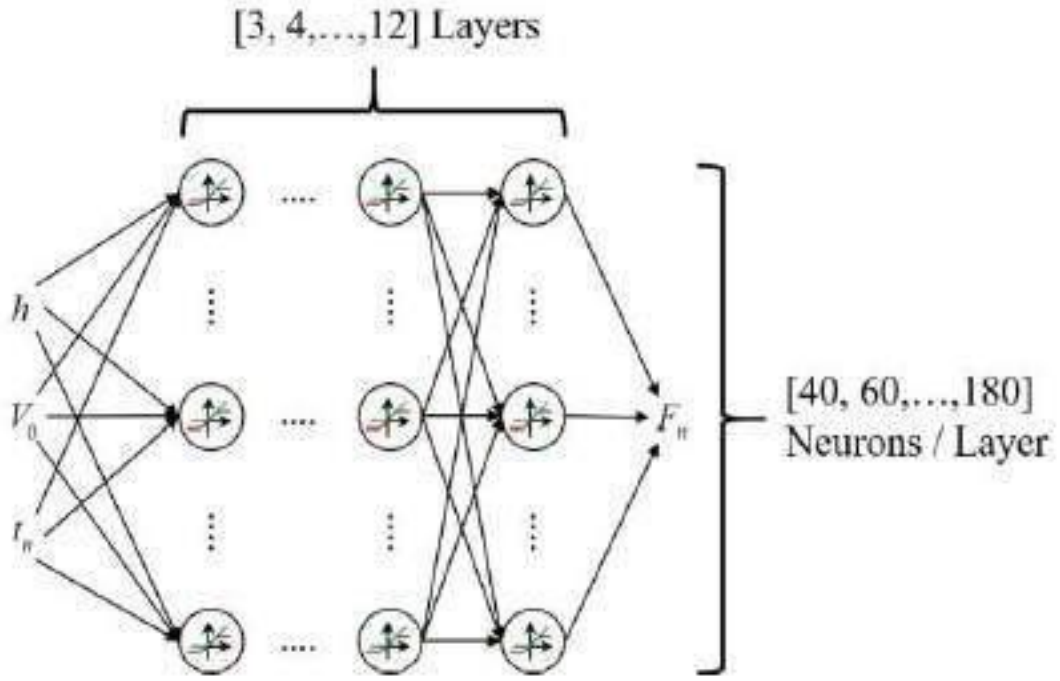

Fig. 3. Basic fully-connected neural network architecture with hyperbolic tangent and/or ReLU activation.

3.2. Training and evaluation scheme

All models are implemented in Python using the Keras interface with the TensorFlow library [37]. We consistently use the ADAM optimizer [38] and the mean absolute error as the loss function across all architectural experiments. A critical preprocessing step involves feature-wise normalization of the input data to a zero mean and unit variance, accomplished with the scikit-learn library [39]. This standardization is necessary because the input features span different scales by orders of magnitude and represent distinct physical quantities. Similarly, the output force values are normalized to the range [0, 1] by division by the maximum observed force. This transformation is inverted during inference by multiplying the network's output by the same maximum value. All other hyperparameters retain their default values. This specific configuration—using ADAM and mean absolute error—was empirically determined to yield better performance than alternatives like SGD, RMSprop, or mean squared error.

The training procedure also involves a carefully chosen batch construction method. The batch size, defining the number of samples processed before a model update, was optimized to balance computational efficiency and gradient estimation accuracy. We found an effective size to be 10 complete force curves, equating to roughly 0.25%

of the training dataset. Crucially, data points for each batch are randomly sampled across multiple curves, meaning a single batch contains random time points from more than 10 different force curves. This randomized batch sampling proved more effective and straightforward to implement than methods using entire consecutive curves or specific time points across all curves. When combined with zero-padding (Section 2.2), this results in a batch size of 50,000 individual data points.

Training is run for an initial 1000 epochs, during which the model processes the entire training set. After each epoch, the validation loss (mean absolute error on the validation set) is computed. Since the validation set is not used for weight updates, this loss serves as an unbiased metric for generalization. An increasing or stagnating validation loss indicates overfitting to the training data. To counter this, we employ an early-stopping callback that does not halt training but instead restores the model's weights to those from the epoch with the lowest validation loss once training concludes. This dynamic selection of the final model, based on validation performance rather than a predetermined epoch count, effectively mitigates overfitting and prevents premature termination due to stochastic fluctuations in the validation loss.

4. Results

4.1. Results from Finite Element Simulations

The results from the finite element simulations, which generated the training data, can be classified into responses dominated by global buckling and those characterized by progressive crushing. Consequently, the visualization of response distributions focuses on these deformation modes and their prevalence across the parametric space. As the crushing mode is a qualitative attribute, a numerical metric is required to represent its distribution automatically. A primary metric, indicative of the axisymmetry of the final deformed tube shape, is defined as:

$$AM = \frac{\sum_{m=1}^{k} \left| l\mathbf{x}_{am} - \sum_{n=1}^{l} \mathbf{x}_{mn} \right|_{t=final}}{\sum_{m=1}^{k} \left| l\mathbf{x}_{am} - \sum_{n=1}^{l} \mathbf{x}_{mn} \right|_{t=initial}}$$

This Axisymmetry Metric (AM) quantifies the average off-axis displacement in the final crushed state. Its formulation leverages the structure of the finite element mesh, which consists of *k* rings, each containing *l* nodes, as illustrated in Fig. 4. In Eq. (4), **xam** denotes the position vector of a point on the tube axis at ring *m*, while **xmn** is the position vector of a node in the mesh. Division by the initial average off-axis

displacement, which is non-zero due to introduced geometric imperfections, normalizes the metric, enabling comparison across tubes of different sizes.

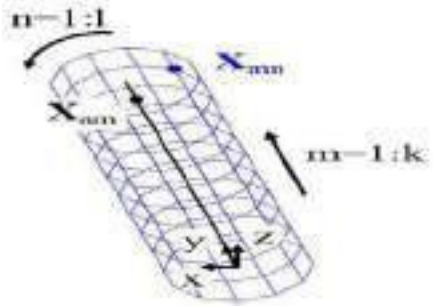

Fig. 4. Geometric definition of the summation indexes used in Eq. (4).

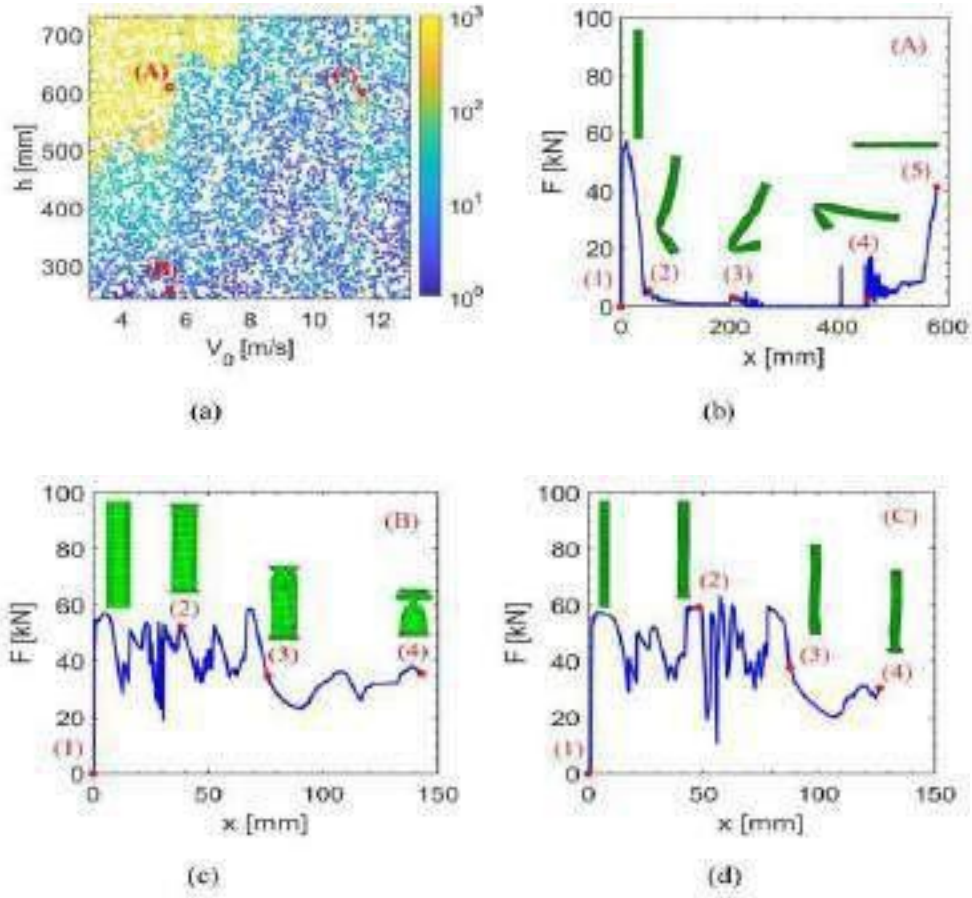

Fig. 5. Distribution of the axisymmetry metric across the entire dataset (a) and indicative crushing responses (b–d).

Since global buckling induces large off-axis displacements, it yields a higher AM value than axial crushing. Figure 5a plots AM against tube height and impact velocity, revealing the distribution and transition between global buckling (yellow) and axial crushing (blue). Corresponding force-displacement curves for selected configurations are shown in Fig. 5b–d. A distinct transition zone in Fig. 5a divides the design space into global buckling and axial crushing regions, a phenomenon consistent with prior observations (Ma et al., 2023). Global buckling primarily occurs in long tubes under low impact velocities, with occasional exceptions where axial crushing appears in the global buckling region and vice versa. This anomalous behavior, also noted in (Sakaridis et al., 2022), is attributed to the imperfection sensitivity of cylindrical structures near the interface region. The consistent replication of these experimentally observed effects provides initial, partial validation for the finite element model used in this study.

The diversity of crushed tube shapes is reflected in their force-displacement curves (Fig. 5b–d). Figure 5b shows a typical global buckling response (point A in Fig. 5a), where the force drops sharply after buckling initiates (point 2). Load values remain low, except for brief spikes from regained contact (point 3), until the top plate nears the bottom. At this stage, the tube is fully collapsed (points 4 and 5), and a final high load peak halts the top plate's motion. For the studied parametric space, this final compaction occurs after approximately 5000 data points, which determined the sampling limit for dataset generation.

Figure 5c illustrates a typical axial crushing response (point B in Fig. 5a). Unlike global buckling, the load does not diminish but fluctuates around a high average value. These fluctuations correspond to the sequential formation of folds, which may initiate near the top plate, bottom plate, or both (points 2 and 3). A variety of fold shapes are observed, including transitions from axisymmetric to non-axisymmetric patterns (point 4), which also alter the character of the force fluctuations.

Figure 5d presents a mixed-mode response (point C in Fig. 5a), featuring elements of both global buckling and axial crushing, as seen in the superimposed deformed shape (points 3 and 4). In such responses, the force-displacement curve may or may not show a load drop due to off-axis displacements. However, suppose displacements become extensive enough to drive the load to near-zero. In that case, it does not recover until the structure is completely bent, similar to the mode in Fig. 5b. Thus, mixed-mode responses fall into two broad categories:

a. Responses where off-axis displacements do not compromise load-bearing capacity. The resulting force-displacement curves are nearly indistinguishable from pure progressive crushing.

b. Responses were global buckling compromises structural integrity. The force-displacement curves here exhibit characteristics of both modes, typically beginning with high-load fluctuations from axial crushing before transitioning to a global buckling phase with a sustained load drop.

4.2. Results from Neural Network Modeling

The results from the neural network modeling are presented in two parts. The first part compares the proposed neural network architectures and details the optimization process, culminating in the identification of the best-performing architecture (hyperparameter identification). The second part provides a quantitative evaluation of this selected model by comparing standard engineering crashworthiness metrics derived from its predictions against those from the finite element models. A baseline for neural network performance is established by also comparing finite element predictions obtained with different levels of structural imperfection.

4.2.1. Hyperparameter Identification

The optimization loss serves as the primary performance indicator, supplemented by considerations of computational cost and the relative performance on training versus validation sets. To account for statistical variance from random weight initialization, each model architecture was trained four times, with reported values representing the average across these runs. Further, to manage computational cost during this hyperparameter search, a subsampled dataset was used, containing only one-tenth of the data points from the full-resolution training, validation, and test sets. This subsampling was found not to significantly alter the optimization loss, provided that all sets were processed consistently. However, as it reduces the fidelity of the predicted curves, this approach was applied only during the hyperparameter identification phase.

The initial architectural comparison investigated the number of layers and the type of activation function. Two neuron-per-layer sizes were tested (60 and 140), with the number of layers varying from 3 to 12, and the activation functions being the Rectified Linear Unit (ReLU) and the hyperbolic tangent (tanh). The average validation losses from these runs are summarized in Fig. 6a. The results demonstrate that increasing the number of hidden layers initially improves performance, regardless of layer size or activation function. However, a threshold exists, between 6 and 9 layers, beyond which adding additional

layers yields diminishing returns or even degrades performance. Regarding activation functions, the tanh function performed better for smaller networks, while the ReLU function was superior for larger architectures. Based on these findings, a configuration with 8 hidden layers and ReLU activation was selected for the subsequent layer size search, as it offered strong performance without excessive computational overhead. The number of neurons per layer was tested from 40 to 180 in steps of 20. Figure 6b shows the evolution of both training and validation loss. Increasing layer size generally improved performance, particularly for the training loss. However, larger networks also exhibited a growing disparity between training and validation loss, indicating overfitting. To balance performance gains with moderate overfitting, the architecture with 100 neurons per layer was chosen for final modeling on the complete, full-resolution dataset.

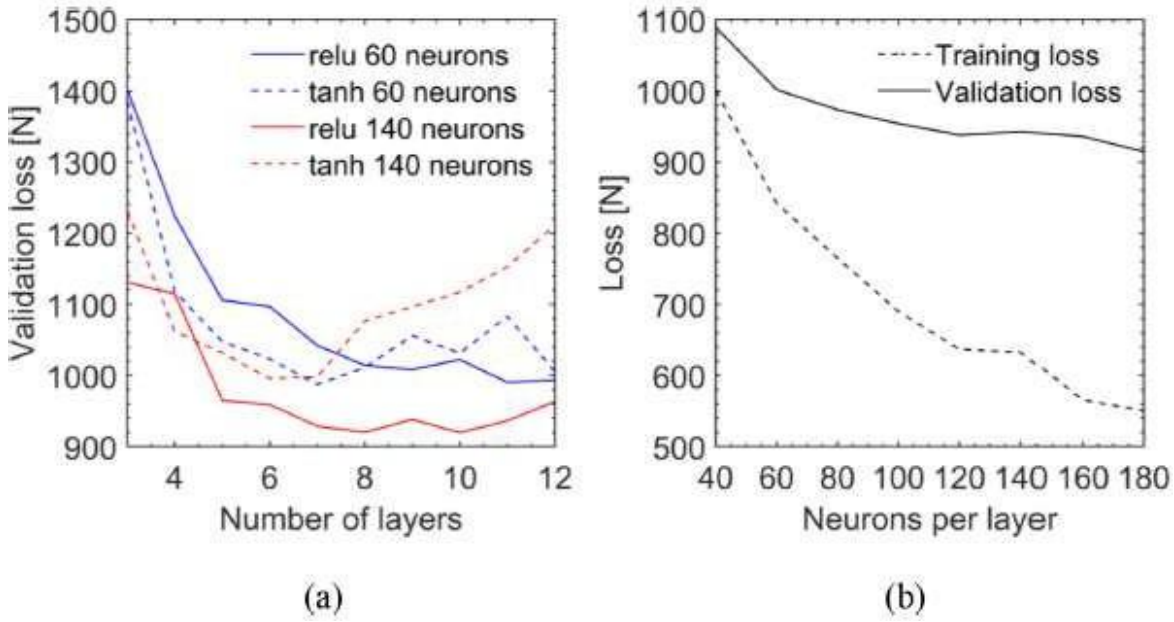

Fig. 6. Hyperparameter tuning results: (a) validation loss versus number of hidden layers; (b) training and validation loss versus number of neurons per layer.

4.2.2. Performance of the calibrated model

The optimized neural network model consists of eight hidden layers, each containing 100 neurons and using ReLU activation functions. This architecture is trained on the full dataset without any form of sub-sampling, which considerably increases the computational effort during both training and inference. Nevertheless, the trained

network can generate predictions for all 5,000 force–time responses in under one minute. In comparison, a conventional explicit finite element (FE) simulation for a single impact scenario typically takes around 15 minutes, and in some cases more than 30 minutes, when executed on a single CPU core. Based on these CPU-only runtimes, the neural network provides a speed-up of at least four orders of magnitude (approximately 10,000×) relative to the FE model. Model accuracy is assessed solely on the test dataset; none of these samples were included in training or validation, ensuring that performance evaluation is free from information leakage or overfitting bias. To quantify the predictive performance of the neural network over the complete force–time history of each impact case, three error measures are defined: (i) maximum load error (MLE), (ii) average load error (ALE), and (iii) absorbed energy error (AEE). Let (F_{FE}(t)) denote the FE-simulated force history and (F_{NN}(t)) the neural network prediction. The MLE is given by

$$MLE = \frac{|\max(F_{NN}(t)) - \max(F_{FE}(t))|}{\max(F_{FE}(t))}.$$

Because peak load typically occurs at the onset of deformation, this metric assesses the model's ability to replicate the rapid changes associated with initial buckling. Figure 7 shows the MLE distribution across the test set, revealing that most peak load predictions fall within a 10% error margin, and numerous cases have sub-0.1% deviation. The distribution is skewed toward scenarios with high impact velocities, where force responses are intrinsically noisier.

The ALE metric evaluates the full-length force response and is defined as

$$ALE = \frac{\sum |F_{NN}(t) - F_{FE}(t)|}{\sum F_{FE}(t)}$$

This normalized error measure is closely related to the loss minimized during training. Although ALE values can be relatively large, occasionally exceeding 100%, the peak of the distribution lies below 10%, and certain cases demonstrate error levels approaching 1%. Higher ALE values tend to occur in regions corresponding to transitions between global buckling and progressive crushing, or at extreme parameter conditions such as high impact speed and small tube height.

The third metric, AEE, reflects errors in predicted total absorbed energy:

$$AEE = \frac{\left|\left(\sum F_{NN}(t)\right)^2 - \left(\sum F_{FE}(t)\right)^2\right|}{\left(\sum F_{FE}(t)\right)^2}$$

As energy absorption is an integral quantity, AEE values are generally lower than ALE values. Most test samples exhibit less than 10% energy error,

with a considerable subset below 0.1%. However, a small number of cases display large errors, particularly in parameter ranges exhibiting transitions between collapse modes, where the network sometimes misidentifies the dominant deformation mechanism. Similar to ALE, high AEE values are more frequent at small tube heights and high crushing velocities.

Overall, while prediction errors are present and, in some cases, sizable, their distribution aligns with known physical behaviors of tube collapse rather than random noise. These systematic patterns suggest that discrepancies arise primarily in complex transition regions of the parameter space. The influence of structural imperfections on these error metrics is examined in the following section.

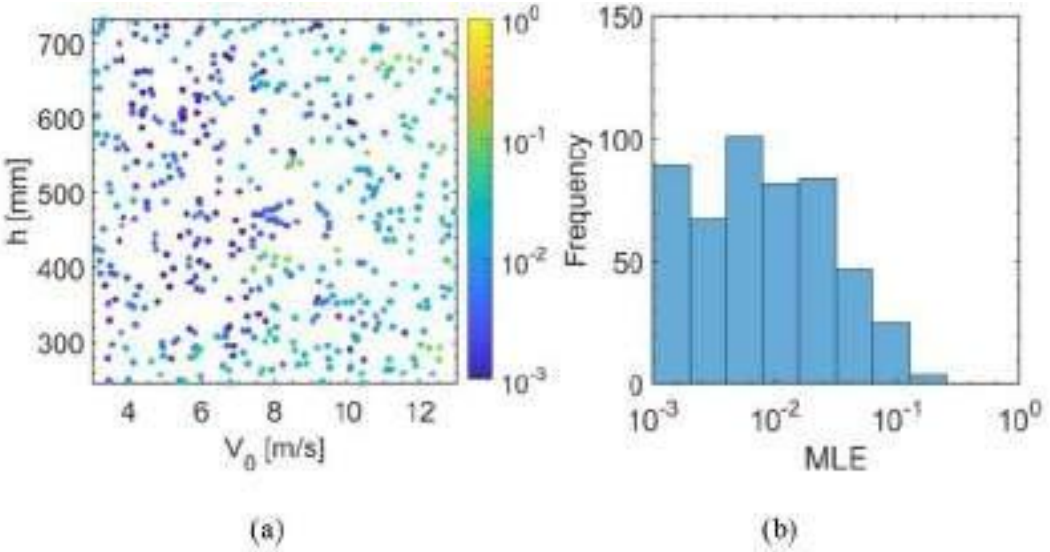

Fig. 7. (a) Distribution of the maximum load error on the test set, (b) histogram of the distribution of the maximum load error on the test set.

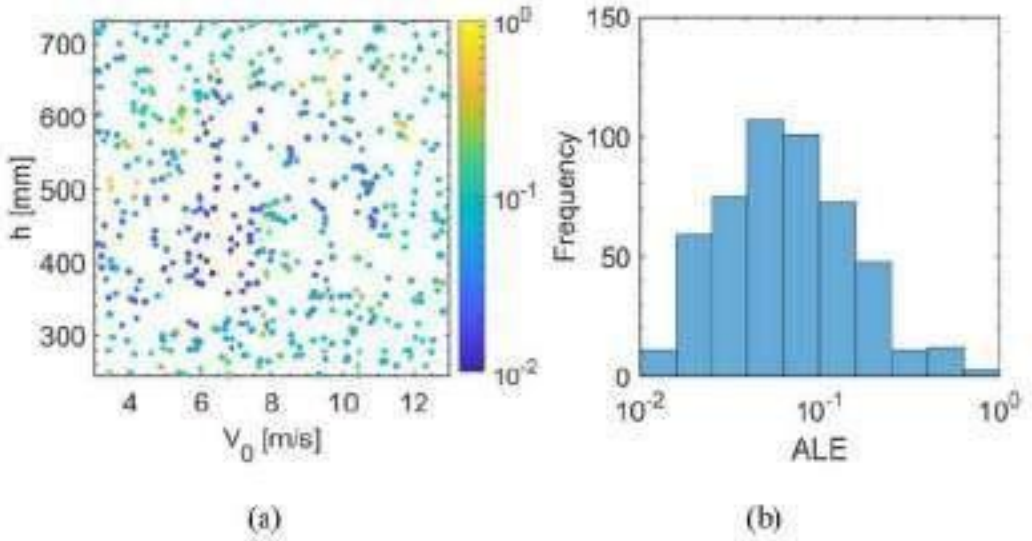

Fig. 8. (a) Distribution of the average load error on the test set, (b) histogram of the distribution of the average load error on the test set.

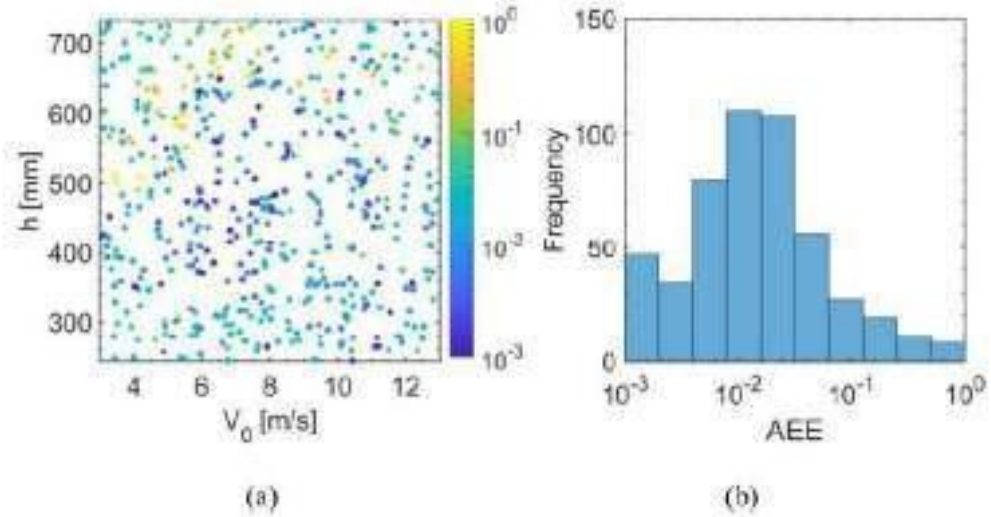

Fig. 9. (a) Distribution of the total absorbed energy error on the test set, (b) histogram of the distribution of the total absorbed energy error on the test set.

4.3. Discussion: effect of geometric imperfections

The amplitude of the original tube waviness, determined with the help of the first elastic buckling mode (Fig. 1), is slightly changed to analyze the effect of geometric imperfections. There are two further sets of finite element simulations made, the first with the imperfection amplitude decreased to 0.000495 h (99 percent of the actual one) and the other with an increase to 0.000505 h (101 percent). Therefore, every force time response of the test set is multiplied thrice with three imperfection magnitudes, with the case of the baseline. Of interest is the fact that a one percent change in the amplitude of the imperfection will lead to the highest dimensional

change of about 3.7 micrometers in the tallest tube taken. These additional simulations are done on the V0 and h combinations of the test set.

In order to measure this impact of imperfection, the three error indices that are utilized in the evaluation of a neural network are used. The formulas are, however, modified to enable direct pair-wise comparison between any two levels of imperfection, i and j. The resulting reformulated expressions of maximum load error, average load error, and absorbed energy error are:

$$MLE_{ij} = 2\frac{\left|\max(F_{FEi}(t)) - \max(F_{FEj}(t))\right|}{\max(F_{FEi}(t)) + \max(F_{FEj}(t))}$$

$$ALE_{ij} = 2\frac{\sum\left|F_{FEi}(t) - F_{FEj}(t)\right|}{\sum F_{FEi}(t) + \sum F_{FEj}(t)}$$

$$AEE_{ij} = 2\frac{\left|\left(\sum F_{FEi}(t)\right)^2 - \left(\sum F_{FEj}(t)\right)^2\right|}{\left(\sum F_{FEi}(t)\right)^2 + \left(\sum F_{FEj}(t)\right)^2}$$

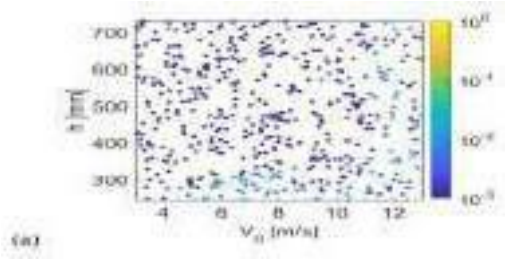

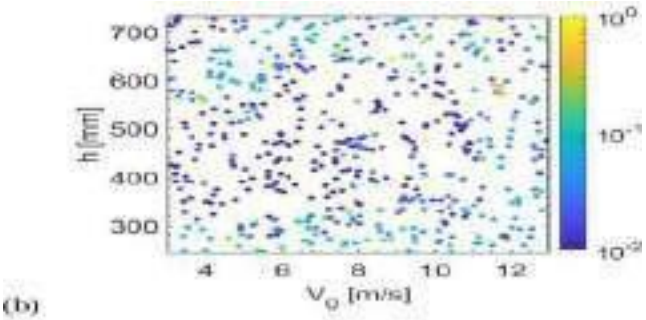

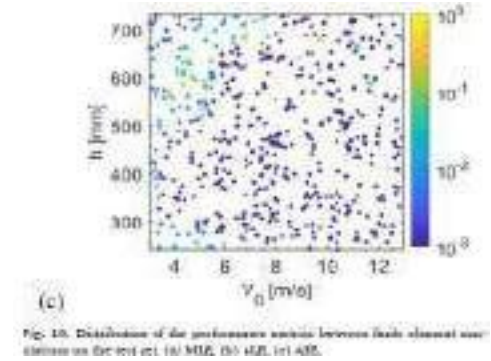

Since there are three imperfection variations in every test set configuration, there are three possible pairwise comparisons, and the metric value reported is the mean of the three possible pairwise comparisons. These error measures are shown in Fig. 10a to 10c. The general tendencies can be compared with those in the neural network error maps (Figs. 7a, 8a, 9a), only that the absolute error values are much lower in cases of the finite element results compared to small changes in imperfections. This is particularly true in terms of peak load and absorbed energy where the financial element simulations indicate near negligence in change. But in some instances, especially in the regions of mode transition, average load change across imperfections is

comparable to the error variances that are realized in the neural network predictions.

Figure 11 also shows the sensitivity of imperfection through overlaying of force histories of selected V0 and h cases. Their positions on the average load error map (Fig. 8a) are shown in Figure 11a, whereas Figure 11b through 11f compares the three finite element responses with A global buckling mode in which the collapse pattern is twisting, is one of the most difficult responses, which is depicted in scenario B (Fig. 11c). The initial response of the neural network is the finite element response, but at the time when the global buckling occurs (30 milliseconds), it starts deviating, then exhibits spurious oscillations and erroneous increase in the late-stage loads. Nevertheless, the network manages to still properly model the peak load and the occurrence of buckling, a fact that is significant since these unusual modes are only loosely represented in the data.

Scenarios C to E (Figs. 11d to 11f) illustrate examples of how small imperfection perturbations can result in apparent divergence among finite element curves, and in extreme cases can shift the collapse mode as was evident in Scenario C. The

the neural network output. Scenario A (Fig. 11b) is an example of an insensitive imperfection case that is far away mode transition boundaries. In this case, the neural network strongly follows the response of the finite element with only slight high-frequency oscillations, meaning it tends to smooth slightly.

difference between the prediction of the neural network and the reference finite element curve is, in such instances, similar to that between the three-imperfection perturbed finite element simulations. In Scenarios C and E, the neural network prediction is closer to one of the other alternate finite element responses as compared to the nominal one. This implies that neural network deviations may indicate actual real physical sensitivity, as opposed to neural network model breakdown.

All these data indicate that the neural network sometimes has strong deviations, but most of such cases are associated with the structural response that is highly sensitive in nature. Thus, huge prediction errors in such areas must be viewed in the framework of inherent physical uncertainty and not only as a weakness of the model.

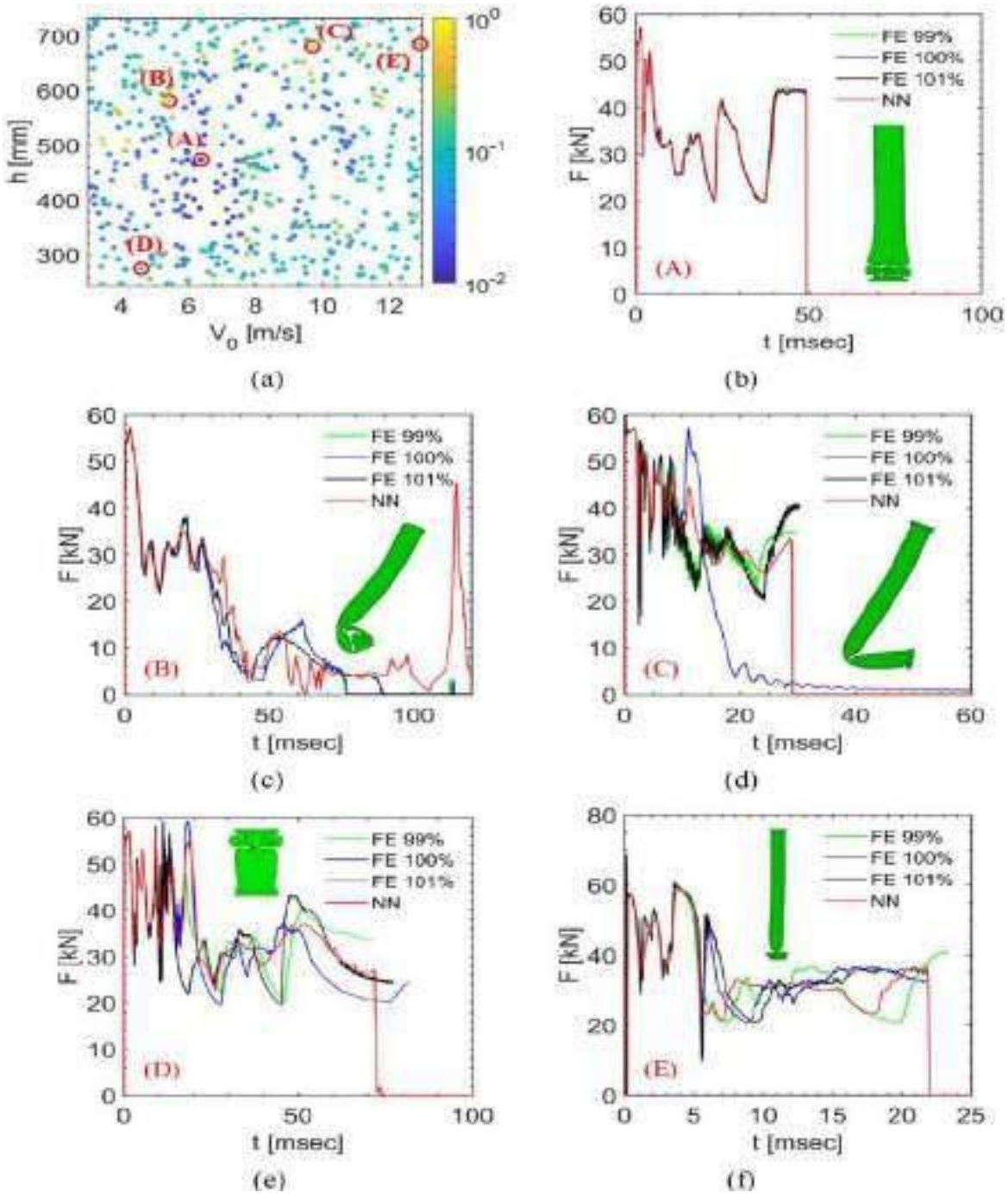

Fig. 11. (a) Indicative [V0, h] pairs superimposed on top of the distribution of the average load error on the test set, (b–f) force time curves from finite element simulations and neural network prediction for the indicative [V0, h] pairs, superimposed with the collapse shape predicted by the original FE simulation (FE-100%). (For interpretation of the references to color in this figure legend, the reader is referred to the web version of this article.

5. Conclusions

Machine-learning-driven framework has been suggested to predict the dynamic crushing behavior and buckling mode transition of tubular structures in axial loading with constant diameter and thickness. Through extensive testing, it was decided that a deep fully connected neural network with eight layers each having 100 neurons and ReLU activation, is able to account crushing response with a high degree of faithfulness. The trained model is more than 10,000 times faster than explicit finite element simulations of shell-based model, and the computational efficacies of the trained model are similar to those of the analytical methods. The error of the model predictions is not erratic; it grows exponentially in the regions of the design space where the deformation mode switches into progressive axial crushing and global buckling, particularly in cases where designs are shorter in tube height, and have a large impact velocity. Extensive studies also found that the geometric imperfections are also more sensitive in these areas. Generally speaking, the neural network is an excellent and effective proxy model, and it can be utilized to model the highly nonlinear and complicated crushing behavior of the thin-walled members in a parameter space of interest. It is proposed in the evidence-of-concept research that comparable machine learning procedures could be extended to more sophisticated structural objects, such as car parts, to simulate impact responses to more comprehensive loading regimes and geometric diversities with much better enhancements in computing velocity besides predictive reliability.

References

Alexander, J. M. (1960). An approximate analysis of the collapse of thin cylindrical shells under axial loading. The Quarterly Journal of Mechanics and Applied Mathematics, 13(1), 10–15. https://doi.org/10.1093/qjmam/13.1.10

Alrowais, R., Alamri, H., & Alqahtani, H. (2023). Application of feed-forward neural networks for structural response prediction in marine and civil structures. Journal of Structural Engineering,

Anand, R., Kumar, V., & Rajan, S. (2024). Analytical evaluation of crush behavior of thin-walled tubes under axial compression. International Journal of Mechanical Sciences,

Ataabadi, S. M., Zarei, H. R., & Sadighi, M. (2022). Numerical simulation of thin-walled tubes under dynamic axial impact using ABAQUS/Explicit. Thin-Walled Structures, 176, 109313.

Gara, F., Pepe, M., & Cerioni, R. (2023). Effects of non-metallic materials on deformation mechanisms of crashworthy structures. Composite Structures, 315, 116885.

Karagiozova, D., Alves, M., & Jones, N. (2000). Inertia effects in axisymmetric progressive buckling of cylindrical shells under axial impact. International Journal of Solids and Structures, 37(29), 3871–3896.

Li, Y., Chen, Z., & Zhao, Y. (2025). Machine-learning-based modeling of anti-climbing crash devices. Engineering Structures,

Ma, H., Jiao, P., Li, H., Cheng, Z., & Chen, Z. (2023). Buckling analyses of thin-walled cylindrical shells subjected to multi-region localized axial compression: experimental and numerical study. Thin-walled structures, 183, 110330.

Najibi, S., Saadatpour, M., & Esmaeili, F. (n.d). Neural-network surrogate modeling for crashworthiness optimization of energy absorbers. Thin-Walled Structures,

Sakaridis, E., Karathanasopoulos, N., & Mohr, D. (2022). Machine-learning based prediction of crash response of tubular structures. International Journal of Impact Engineering, 166, 104240.

Sakaridis, I., Gkantou, M., & Gardner, L. (2022). Recurrent neural networks in civil engineering for dynamic response prediction. Engineering Structures, 260, 114236.

Schneider, M., Mueller, R., & Habib, A. (2022). Computational bottlenecks in high-fidelity finite element simulations of dynamic buckling. Finite Elements in Analysis and Design, 208, 103844.

Sun, G., Wang, H., & Li, Q. (2021). Critical buckling length and crushing performance of circular tubes under dynamic impact. International Journal of Mechanical Sciences, 197, 106353.

Sun, G., Wang, H., & Li, Q. (2025). Optimization of complex energy-absorbing structures under dynamic loading using surrogate models. Thin-Walled Structures, —, —.

Wang, Z., Zhang, X., & Liu, P. (2022). Plastic deformation behavior of thin-walled tubes for impact energy absorption. International Journal of Impact Engineering, 169, 104324.

Xu, L., Liu, J., & Fang, H. (2023). Energy absorption mechanisms in thin-walled tubular structures for automotive safety. Engineering Structures, 290, 116270.

Zeng, Y., Zhou, H., & Chen, X. (2024). Fully-connected neural networks for crashworthiness prediction of parametrized structures. Computers & Structures, 287, 107183.

Zhang, C., Hu, J., & Huang, Y. (2025). Analytical models for fold formation and deformation modes in thin-walled tubes. International Journal of Mechanical Sciences,

Zhang, C., Huang, Y., & Hu, J. (2021). Buckling mode transition in circular tubes under dynamic axial compression. Thin-Walled Structures, 167, 108105.